Free infragravity waves in the North Sea

Dirk Pieter Rijnsdorp[1], Adrianus Reniers[2], and Marcel Zijlema[3]

[1]Delft University of Technology
[2]University of Miami
[3]Delft University of Technology,Delft University of Technology

November 26, 2022

Abstract

Infragravity waves are low-frequency surface waves that can impact a variety of nearshore and oceanic processes. Recent measurements in the North Sea showed that significant bursts of infragravity energy occurred during storm events. Using a spectral wave model, we show that a substantial part of this energy was radiated from distant shorelines where it was generated by the incident sea-swell waves. These radiated infragravity waves can cross the sea basin and reach distant shorelines where they add to locally generated infragravity waves that are trapped by refraction. During storms, the shoreward directed component of the infragravity waves can reach up to O(0.5) m in height along the coastline, suggesting that they can potentially impact the coastal environment of the North Sea.

Free infragravity waves in the North Sea

Dirk P. Rijnsdorp[1], Ad J. H. M. Reniers[1], Marcel Zijlema[1]

[1]Environmental Fluid Mechanics section, department of Hydraulic Engineering, Faculty of Civil Engineering and Geosciences, Delft University of Technology, Delft, the Netherlands

Key Points:

- Significant bursts of free infragravity energy in the North Sea can be explained by radiation from distant shorelines
- The origin of the free infragravity waves depends on storm intensity and track, and particularly where largest sea-swell waves make landfall
- The shoreward directed free infragravity waves can reach heights up to 0.6 m, suggesting that they may impact the coastal environment

Corresponding author: Dirk P. Rijnsdorp, d.p.rijnsdorp@tudelft.nl

Abstract

Infragravity waves are low-frequency surface waves that can impact a variety of nearshore and oceanic processes. Recent measurements in the North Sea showed that significant bursts of infragravity energy occurred during storm events. Using a spectral wave model, we show that a substantial part of this energy was radiated from distant shorelines where it was generated by the incident sea-swell waves. These radiated infragravity waves can cross the sea basin and reach distant shorelines where they add to locally generated infragravity waves that are trapped by refraction. During storms, the shoreward directed component of the infragravity waves can reach up to $\mathcal{O}(0.5)$ m in height along the coastline, suggesting that they can potentially impact the coastal environment of the North Sea.

Plain Language Summary

Infragravity waves are long period surface waves that are small in the ocean but much larger in the shallow waters closer to the coast. In coastal regions, they are known to affect coastal safety assessments as they can, for example, impact the overtopping of coastal structures, enhance the erosion of dunes, and trigger the resonance of harbours. To date, such assessments have typically assumed that these infragravity waves were locally generated by sea-swell waves (waves generated by the wind). Recent observations in the North Sea showed that large infragravity waves occurred during storm events. By analyzing the measurements and using a wave model, we have shown that a substantial part of these waves was not generated locally but originated from distant shorelines. At such a distant shoreline, infragravity waves were generated by the breaking of sea-swell waves at the beach. After generation, the infragravity waves radiate into the sea, and our modelling shows that they are able to cross the North Sea and reach distant shorelines. Here, they combine with locally radiated infragravity waves. Our study suggests that these radiated infragravity waves can be of substantial height during storm events, and may impact the coastal environment of the North Sea.

1 Introduction

Infragravity (IG) waves are longer period surface gravity waves with typical frequencies ranging between 0.005-0.05 Hz. They are typically considered small in oceanic waters with heights of $\mathcal{O}$(cm) (e.g., Webb et al., 1991; Aucan & Ardhuin, 2013), but can reach heights up to $\mathcal{O}$(m) in shallow water during severe weather events (e.g., Sheremet et al., 2014; Matsuba et al., 2020). In the past decades it has been well established that IG waves contribute to various nearshore processes, such as nearshore hydrodynamics (e.g., Guza & Thornton, 1985; Henderson & Bowen, 2002; Pomeroy et al., 2012), sediment transport (e.g., Aagaard & Greenwood, 1994; de Bakker et al., 2016), and erosion of beaches and dunes (e.g., Russell, 1993; Van Thiel de Vries et al., 2008). Associated with their longer periods, they can also trigger harbour seiches (e.g., Bowers, 1977; Okihiro et al., 1993; Thotagamuwage & Pattiaratchi, 2014; Cuomo & Guza, 2017) and excite large motions of moored vessels (e.g., Van der Molen et al., 2006; van der Molen et al., 2016). Despite their relative small amplitude in deeper water, they have been found to be the source of seismic hum (e.g., Rhie & Romanowicz, 2006; Webb, 2007; Ardhuin et al., 2015) and may impact the integrity of ice-shelves in polar regions (e.g., Bromirski et al., 2010, 2015).

IG waves are generally considered to result from the interactions among wind-generated (sea-swell) surface gravity waves (e.g., Longuet-Higgins & Stewart, 1962; Hasselmann, 1962), see Bertin et al. (2018) for a recent review. The strength of these interactions is depth dependant and only become significant (i.e., approach resonance) in shallow water, resulting in negligible forced IG waves in oceanic water. In the surfzone, the (near) resonant interactions combined with other generation mechanisms (e.g., Symonds et al., 1982) result in a substantial transfer of energy from the sea-swell to the IG frequencies. After (partial) reflection at the shoreline (e.g., Battjes et al., 2004; Van Dongeren et al., 2007; De Bakker et al., 2014), free infragravity (FIG) waves that are no longer bound to their forcing radiate seaward into oceanic basins and onto the shelf (e.g., Herbers, Elgar, Guza, & O'Reilly, 1995; Herbers, Elgar, & Guza, 1995). FIG energy levels reduce in deeper water due to refractive trapping (e.g., Gallagher, 1971; Okihiro et al., 1992; Herbers, Elgar, & Guza, 1995), limiting their radiation into ocean basins (e.g., Smit et al., 2018). Nonetheless, part of the FIG energy can reach and cross ocean basins (e.g. Rawat et al., 2014; Crawford et al., 2015; Neale et al., 2015; Bogiatzis et al., 2020), where it can explain the majority of the energy at IG frequencies due to weak (non-resonant) local forcing by sea-swell waves. Other generation mechanics in deep water have also been proposed, such as atmospheric forcing by wind speed fluctuations (de Jong & Battjes, 2004; Vrećica et al., 2019) and IG-tidal interactions (Sugioka et al., 2010), but – to date – most of the IG energy in intermediate and deep water has been explained by FIG radiation from distant shorelines.

Recent analysis of measurements in intermediate water depths (approx. 30 m) of the southern North Sea showed significant bursts of IG energy during storm events (Reniers et al., 2021). Only part of this energy could be attributed to local forcing from sea-swell (ranging between 10-100% depending on geographic location and timing relative to the peak of the storm). As a result, the source and origin of a substantial part of the IG energy remains unclear. The objective of this paper is to understand the dominant source and origin of this FIG energy for four of the most severe storm events in the observational record. We use the spectral wave model SWAN (Booij et al., 1999) extended with an empirical source of FIG energy along the shoreline (Ardhuin et al., 2014) to determine the contribution from FIG radiated from the coastlines bordering the North Sea (described in Section 2). Model-data comparisons at the three available measurement stations show that most of the FIG energy can be explained by radiation from distant shorelines (Section 3). In section 3.4, the model results are further analysed to gain insight into the onshore component of the FIG energy along the coastlines of the southern North Sea. This is followed by a discussion of the main conclusions of this work (Section 4).

2 Methods

2.1 Observations

Between 2010-2018, significant bursts of IG energy were observed during storm events at three measurement stations located in the intermediate water depths (approximately 30 m) of the southern North Sea (Reniers et al., 2021). At such intermediate water depths, both FIG and bound IG waves (locally forced by the sea-swell waves) may contribute to energy at the IG frequencies. Decomposing the total IG energy into bound and free components indicated that a substantial part of the energy could not be attributed to local forcing from sea-swell waves.

The contribution by bound IG waves was estimated using second-order equilibrium theory (Hasselmann, 1962) based on measured directional sea-swell spectra. The contribution from FIG was subsequently estimated by subtracting the predicted bound IG spectrum $E_b(f)$ from the measured IG spectrum $E(f)$. The FIG wave height H_{FIG} was computed by integrating the resulting spectrum over the IG frequency band (due to measurement limitations only lower IG frequencies were available, $0.005 \leq f \leq 0.01$ Hz),

$$H_{FIG} = 4\sqrt{\int_{0.005}^{0.01} \left(E(f) - E_b(f)\right) \mathrm{d}f} \tag{1}$$

2.2 Model

The spectral wave model SWAN was used to simulate the temporal and spatial evolution of FIG waves that were radiated from the shorelines bordering the North Sea. To account for the radiation of FIG waves from the shoreline, the SWAN model was extended with an empirical source of FIG energy following the approach of Ardhuin et al. (2014). The empirical source is based on a parametrization that prescribes the bulk IG wave height based on local sea-swell wave parameters (taken seaward from the surf-zone). This parametrization provided a good correlation at several locations in moderate to deep water (Ardhuin et al., 2014). Combined with an empirical spectral shape and isotropic directional distribution, the FIG source is given by,

$$E(f,\theta) = 1.2\alpha_1^2 \frac{kg^2}{c_g 2\pi f} \left(\frac{1}{4} H_{m0} T_{m0,-2}\right)^2 \times \frac{1}{\Delta_f} \left(\min\left(1., 0.015/f\right)\right)^{1.5} \times \frac{1}{2\pi}, \tag{2}$$

in which f is the wave frequency, k is the wave number, c_g is the group velocity, and Δ_f ensures that the frequency distribution integrates to 1. H_{m0} is the sea-swell significant wave height, $T_{m0,-2}$ is a sea-swell mean wave period, and α_1 is a (dimensional) calibration parameter. The source term can be imposed along waters of variable depth as the term $kg^2/c_g 2\pi f$ accounts for the shoaling of a directional broad wave spectrum (Ardhuin et al., 2014).

The IG source term was implemented as part of the obstacle functionality in SWAN, by which a line can be specified along which FIG energy should be radiated. In this work, we impose the IG source at intermediate water depths (≈ 15 m) along all coastlines that border the North Sea. In regions with complex shorelines, such as the Scheldt estuary and the Wadden Sea, the source was occasionally located in waters of 10 m depth. In regions with steep and irregular coastlines (e.g., along the Norwegian coast), the source term was located in water depths of ≈ 20 m.

The SWAN model was run in nonstationary mode with a spatial resolution of 0.025° and 0.0165° in longitudinal and latitudinal direction, respectively, a directional resolution of 8° and a time step of 1 hr. Twenty-five discrete frequencies with default logarithmic spacing were used to discretize the IG frequency band ($0.005 \leq f \leq 0.05$ Hz). The spatial and directional resolutions were found to be sufficient based on sensitivity tests (refer to the Supporting Information for more details). Reducing the time-step did not affect the model results (not shown). No additional source terms were included in the simulations, except for dissipation due to bottom friction using the JONSWAP formulation of Hasselmann et al. (1973). To understand the origin of the FIG waves in the North Sea, additional simulations were run with the same model-setup, but with a subset of coastlines radiating IG energy. Individual simulations were conducted with IG waves radiating from only the Belgium, Dutch, German, Danish, UK, or Norwegian coast.

The sea-swell wave height H_{m0} and mean wave period $T_{m0,-1}$ (due to unavailability of $T_{m0,-2}$) of Eq. 2 were obtained from the global ECMWF ERA5 reanalysis (Hersbach et al., 2020). These bulk wave parameter were available every hour at a 0.5° resolution, and were interpolated to the depths at which the IG source was specified. The α_1 parameter and the bottom friction coefficient were set based on a calibration study for a single storm event (storm Friedhelm) during which the majority of radiated FIG energy originated from the Danish coast (refer to the Supporting Information for more details). Satisfactory results were obtained for $\alpha_1 = 18 \times 10^{-4}$ s^{-1}, which is of the same order of magnitude as the values used in Ardhuin et al. (2014) and Rawat et al. (2014), in combination with a bottom friction coefficient of $\chi = 0.01$ m^{2}s^{-3}. This bottom friction coefficient is lower than the default value $\chi = 0.038$ m^{2}s^{-3} typically used for sea-swell waves (e.g., Zijlema et al., 2012). To study the influence of bottom friction, additional simulations without bottom friction were conducted, for which the calibration study indicated optimal results for a slightly smaller α_1 value of 14.4×10^{-4} s^{-1}. In this work, a constant α_1 was used for all shorelines, and no attempt was made to optimise α_1 by varying it for different shorelines to account for differences between geographic regions (e.g., steep versus mild bottom slopes) that may affect FIG radiation.

The SWAN model was used to hindcast four storm events that resulted in the largest observed H_{FIG} at the three measurement stations (storm Friedhelm, 8-11 Dec 2011; Xaver, 5-8 Dec 2013; Axel, 4-5 Jan 2017; and Egon, 13-15 Jan 2017). Directional spectra were outputted at the three measurement stations and along the shorelines bordering the southern North Sea (at approximately 20 m depth). The predicted H_{FIG} was computed by integrating the directional spectra from SWAN over all directions and the IG frequency band. When comparing model results with measurements, spectra were integrated over the measured IG frequency band (0.005 Hz $\leq f \leq$ 0.01 Hz).

3 Results

3.1 Storm Xaver

In Dec 2013, a severe winter storm tracked from north of the UK towards the south of Norway and north of Denmark. Significant sea-swell wave heights H_{SS} in the central North Sea at station A12 reached 8 m with mean sea swell periods $T_{m0,-1}$ exceeding 10 s (Fig. 1c), with largest sea-swell waves occurring in the northern part of the North Sea (e.g., Fig. 1a). Storm Xaver produced the largest IG response in the observational record at A12, with FIG heights $H_{FIG} > 0.2$ m for approximately 24 h (Fig. 1d). H_{FIG} was lower but still significant at stations Q1 and EUR, which are located further southward and in closer vicinity to the Dutch coast. During this storm event, FIG waves contributed significantly to the total IG variance (compare full and dashed lines in Fig. 1d, and see also Fig. 4 in Reniers et al. (2021)).

In accordance with the measurements (Fig. 1d), the predicted FIG wave heights showed great spatial variability in the North Sea (e.g., during the peak of the storm (06:00 UTC 6 Dec, Fig. 1b). Largest H_{FIG} typically occurred near the Danish coast due to local radiation, and H_{FIG} decreased for an increasing distance away from the Danish coast. H_{FIG} was amplified by shoaling in regions of relatively shallow water, such as near the Dogger and Norfolk banks.

Predicted H_{FIG} captured the typical magnitude and trend of the observations at the three stations (Fig. 1d), which indicates that the observed FIG levels can be partly explained by IG wave radiation from neighbouring shorelines. The model failed to capture relatively large H_{FIG} at A12 prior to the peak of the storm (00:00 UTC 6 Dec), indicating that FIG wave radiation from surrounding beaches cannot explain these FIG energy levels. We will return to this in Section 3.3.

The model simulations further allow us to understand the temporal and spatial variability in H_{FIG} by considering the origin of the IG energy. For the majority of the storm, the modelled H_{FIG} at A12 primarily originated from the Danish coast (Fig. 1e), which can be explained by the occurrence of the largest sea-swell waves in the northern part of the North Sea (Fig. 1a). At Q1 and EUR however, most of the modelled IG variance originated from the Dutch coast (Fig. 1f-g), with a smaller but non-negligible contribution from the Danish coast ($\approx 10 - 20\%$ of the FIG variance). This further illustrates how FIG waves radiated from the Danish coast were attenuated by the combined effect of refraction and dissipation by bottom friction before they reached these stations in the southern North Sea (we will return to the effect of bottom friction in Section 3.3).

3.2 Storm Egon

During storm Egon, large sea-swell waves occurred between 13 and 15 Jan, with H_{SS} up to 8 m at A12, and with H_{SS} peaking at 5 m at EUR in the southern North Sea. Storm Egon was preceded by another storm (11-13 Jan), with weaker but still significant waves ($H_{SS} > 4$ m) at A12 and Q1. Between 11-13 Jan, FIG patterns were comparable to storm Xaver with largest H_{FIG} at A12 and progressively smaller H_{FIG} towards the south at Q1 and EUR. During storm Egon (13-15 Jan) on the other hand, H_{FIG} was generally largest at Q1 and smallest at A12.

The model captured the typical magnitude of H_{FIG} at all three stations, except for large H_{FIG} at A12 prior to the peak of both storms (similar to the findings for storm Xaver). Notably, the model captured the trends in H_{FIG} that occurred during the first (largest H_{FIG} at A12) and second storm event (largest H_{FIG} at Q1). The general agreement between the model and the observations indicates that a significant part of the IG energy can be attributed to the arrival of FIG waves that were radiated from nearby shorelines.

During the first storm (11-13 Jan) modelled H_{FIG} at A12 mainly originated from Denmark, whereas between 13-15 Jan, H_{FIG} was primarily explained by contributions from Denmark and the UK. The modelling results thus suggest that the variability in H_{FIG} (largest H_{FIG} at A12 between 11-13 Jan and largest H_{FIG} at Q1 between 13-15 Jan) is related to the storm trajectory and the spatial variability of the sea-swell waves, with stronger IG radiation from the Danish coast between 11-13 Jan due to a more northerly storm track, and stronger IG radiation along the shorelines of the southern North Sea (UK and NL) between 13-15 Jan due to a more southerly storm track.

3.3 All storms and the influence of bottom friction

Comparing the observed and modelled H_{FIG} at all stations for all considered storm events shows that the model (including bottom friction) generally reproduced the observations (Fig. 3). The agreement was best at Q1 and EURO, where the model Skill indicates that the model explained 75% of the variability in the FIG wave height (Fig. 3 b-c). At these stations, the model suggests that the FIG variance was typically dominated by radiation from the nearby Dutch coast (Fig. 3 e-f).

The agreement at A12 was poorer (Fig. 3 a), with a lower Skill and larger Relative Bias (RB) consistent with a typical under prediction of H_{FIG}. This under prediction at A12 occurred consistently at times prior to the peak of all four storms (blue markers in Fig. 3a), as was observed previously for storm Xaver and Egon (Fig. 1-2). Near and following the peak of the storm (gray to red markers in Fig. 3a), the model did capture H_{FIG}, suggesting that at these time the observed FIG waves originated from surrounding shorelines. At station A12, the modelled FIG variance was typically dominated by radiation from the Danish coast (Fig. 3d).

The model-data mismatch at A12 prior to the peak of the storm indicates that radiation from surrounding shorelines cannot explain these FIG energy levels. This suggests that other physical mechanisms could be at play. At times of the unexplained FIG energy, the sea-swell waves typically originated from WNW to NNW and passed the Dogger Bank (a shallow shoal located in the central North Sea) prior to reaching station A12 (which is located on the south-eastern side of the Dogger Bank). Although the precise generation mechanism remains unclear, this indicates that the unexplained energy in the IG band could originate from local excitation of FIG waves by sea-swell waves as they pass over the shallow shoal (e.g., Molin, 1982; Mei & Benmoussa, 1984; Li et al., 2020; Contardo et al., 2021).

To study the influence by bottom friction, the SWAN simulations were repeated excluding this source term and a slightly lower α_1 value (to compensate for the absence of dissipation by bottom friction). The influence of bottom friction on H_{FIG} is particularly notable at stations Q1 and EUR, where it reduced the Danish contribution at times that significant IG variance originated from Denmark (Fig. 3e-f versus Fig. 3k-i), resulting in a minor improvement of the overall model skill. These results indicate that bottom friction can provide some additional attenuation of FIG waves as they propagate through the relatively shallow North Sea basin. For the four storms considered, the bottom friction only led to noticeable attenuation when most FIG energy originated from the Danish coast.

3.4 Shoreward directed FIG energy

The results in the previous subsections did not consider the full IG frequency band (due to measurement limitations) and focused on three stations in intermediate water depths of the southern North Sea. To gain insight into the potential magnitude of FIG energy that is incident to the coastlines, two-dimensional spectra were outputted at approximately 20 m depth along the coastlines bordering the southern North Sea. Incident FIG wave heights were computed by integrating the SWAN spectra over the full IG frequency band and the shoreward directed directional bins,

$$H^{+}_{FIG} = \int_{0.005}^{0.05} \int_{\theta_p-90^\circ}^{\theta_p+90^\circ} E(f,\theta)\mathrm{d}\theta\mathrm{d}f, \tag{3}$$

in which θ_p is the angle perpendicular to the shore.

Fig. 4 shows the maximum H^{+}_{FIG} that occurred during each of the four storms (top to bottom panels) along the UK coastline (left panels) and the coastline between Belgium and Denmark (right panels). The maximum H^{+}_{FIG} shows a strong spatial variation along the coast of western Europe (Fig. 4), with typically largest H^{+}_{FIG} of up to 0.6 m along the Danish coast. Here, H^{+}_{FIG} was primarily explained by IG energy from local origin (refractive trapping), associated with significant local radiation due to large sea-swell waves along the Danish coast (especially during storm Friedhelm and Xaver).

The maximum H^{+}_{FIG} decreased towards the south (from the German to the Belgian coast), with a decreasing contribution from the Danish coast (associated with increased attenuation due to refraction and bottom friction). Along the Belgian to German coast, the maximum H^{+}_{FIG} was of mixed origin, with different major contributing shorelines depending on where significant sea-swell waves made landfall during the particular storm. Along the UK coast, the maximum H^{+}_{FIG} was of similar magnitude as along the Belgian and Dutch coast, with small contribution from local radiation as the UK coast lacked exposure to significant sea-swell waves during these four storms (associated with a typical north to east storm track). Nonetheless, the maximum H^{+}_{FIG} along the UK coast reached up to 0.2-0.3 m due to arrival of FIG waves from remote shorelines (e.g., from Denmark during storm Friedhelm Fig. 4a, and from the Netherlands during storm Egon at lower latitudes, Fig. 4g).

4 Discussion and conclusions

In-situ observations at three measurement stations in the southern North Sea revealed the occurrence of substantial bursts of free infragravity wave energy during four significant storm events. A spectral wave model that accounts for the radiation of FIG waves from adjacent beaches was able to explain up to 75% of the observed variability in the FIG wave height. The model captured the typical magnitude and temporal variation of the FIG wave height at the three measurement stations. Although the model failed to explain significant FIG energy levels that occurred prior to the peak of storms at the measurement site in the central North Sea (suggesting that other processes also contributed to FIG energy at this location), the overall model-data agreement suggests that a significant fraction of the FIG energy levels in the southern North Sea originated from distant shorelines. These results are in accordance with previous studies on the shelf (Smit et al., 2018) and in the deep ocean (e.g., Rawat et al., 2014; Crawford et al., 2015; Neale et al., 2015; Bogiatzis et al., 2020) that linked significant energy at IG frequencies to radiation of FIG from distant shorelines.

The origin of the FIG energy in the southern North Sea was found to depend on the storm characteristics, and in particular on where large sea-swell waves made landfall. The model suggests that radiated FIG energy was able to cross the North Sea basin and reach neighbouring shorelines, where it adds to FIG energy with a local origin (regionally trapped due to refraction). The FIG energy levels from a distant source were attenuated by refraction and bottom friction, and the predicted nearshore FIG energy levels were typically dominated by waves with a local origin. Along the coastlines at approximately 20 m depth, the model showed that during storms the shoreward directed component of the FIG waves can reach up to 0.6 m in height, which suggests that FIG waves can potentially impact the coastal environment in the North Sea and influence processes like flooding, dune erosion, and seiching of harbours.

Acknowledgments

This research is part of the “Kennis voor Keringen”, research for flood defenses program of Rijkswaterstaat, part of the Ministry of Infrastructure and Water Management. We thank Robert Slomp and Robert Vos for supporting this research. The ERA5 reanalysis is publicly available from the Climate Data Store of the Copernicus Climate Change Service (`https://doi.org/10.24381/cds.adbb2d47`). The measured infragravity wave data set and the source code of the adapted SWAN model are available from `https://surfdrive.surf.nl/files/index.php/s/dITA6eD1r4iFxDj`. Upon publication, the data set and the source code will be made available through the 4TU.ResearchData repository (`https://data.4tu.nl/repository`). We thank Deltares and Rijkswaterstaat for providing the SWAN-DCSM model schematisation (SWAN-DCSM-j15-v1).

References

Aagaard, T., & Greenwood, B. (1994). Suspended sediment transport and the role of infragravity waves in a barred surf zone. *Marine Geology*, *118*(1-2), 23–48. doi: 10.1016/0025-3227(94)90111-2

Ardhuin, F., Gualtieri, L., & Stutzmann, E. (2015). How ocean waves rock the Earth: Two mechanisms explain microseisms with periods 3 to 300s. *Geophysical Research Letters*, *42*(3), 765–772. doi: 10.1002/2014GL062782

Ardhuin, F., Rawat, A., & Aucan, J. (2014, 5). A numerical model for free infragravity waves: Definition and validation at regional and global scales. *Ocean Modelling*, *77*, 20–32. Retrieved from `http://linkinghub.elsevier.com/retrieve/pii/S1463500314000274http://www.sciencedirect.com/science/article/pii/S1463500314000274` doi: 10.1016/j.ocemod.2014.02.006

Aucan, J., & Ardhuin, F. (2013, 7). Infragravity waves in the deep ocean: An upward revision. *Geophysical Research Letters*, *40*(13), 3435–3439. Retrieved from `http://doi.wiley.com/10.1002/grl.50321` doi: 10.1002/grl.50321

Battjes, J. A., Bakkenes, H. J., Janssen, T. T., & Van Dongeren, A. R. (2004). Shoaling of subharmonic gravity waves. *Journal of Geophysical Research*, *109*(C2). Retrieved from `http://doi.wiley.com/10.1029/2003JC001863` doi: 10.1029/2003JC001863

Bertin, X., Bakker, A. d., Dongeren, A. v., Coco, G., André, G., Ardhuin, F., ... Tissier, M. (2018, 1). Infragravity waves: from driving mechanisms to impacts. *Earth-Science Reviews*. Retrieved from http://linkinghub.elsevier.com/retrieve/pii/S0012825217303239 doi: 10.1016/j.earscirev.2018.01.002

Bogiatzis, P., Karamitrou, A., Ward Neale, J., Harmon, N., Rychert, C. A., & Srokosz, M. (2020, 6). Source Regions of Infragravity Waves Recorded at the Bottom of the Equatorial Atlantic Ocean, Using OBS of the PI-LAB Experiment. *Journal of Geophysical Research: Oceans*, *125*(6), 1–17. Retrieved from https://onlinelibrary.wiley.com/doi/abs/10.1029/2019JC015430 doi: 10.1029/2019JC015430

Booij, N., Ris, R. C., & Holthuijsen, L. H. (1999). A third-generation wave model for coastal regions: 1. Model description and validation. *Journal of Geophysical Research*, *104*(C4), 7649–7666. Retrieved from http://doi.wiley.com/10.1029/98JC02622 doi: 10.1029/98JC02622

Bowers, E. C. (1977, 4). Harbour resonance due to set-down beneath wave groups. *Journal of Fluid Mechanics*, *79*(1), 71–92. Retrieved from http://www.journals.cambridge.org/abstract_S0022112077000044 doi: 10.1017/S0022112077000044

Bromirski, P. D., Diez, A., Gerstoft, P., Stephen, R. A., Bolmer, T., Wiens, D. A., ... Nyblade, A. (2015). Ross ice shelf vibrations. *Geophysical Research Letters*, *42*(18), 7589–7597. doi: 10.1002/2015GL065284

Bromirski, P. D., Sergienko, O. V., & MacAyeal, D. R. (2010, 1). Transoceanic infragravity waves impacting Antarctic ice shelves. *Geophysical Research Letters*, *37*(2). Retrieved from http://doi.wiley.com/10.1029/2009GL041488 doi: 10.1029/2009GL041488

Contardo, S., Lowe, R. J., Hansen, J. E., Rijnsdorp, D. P., Dufois, F., & Symonds, G. (2021, 2). Free and forced components of shoaling long waves in the absence of short wave breaking. *Journal of Physical Oceanography*. Retrieved from https://journals.ametsoc.org/view/journals/phoc/aop/JPO-D-20-0214.1/JPO-D-20-0214.1.xml doi: 10.1175/JPO-D-20-0214.1

Crawford, W., Ballu, V., Bertin, X., & Karpytchev, M. (2015, 7). The sources of deep ocean infragravity waves observed in the North Atlantic Ocean. *Journal of Geophysical Research: Oceans*, *120*(7), 5120–5133. Retrieved from http://www.nature.com/articles/175238c0http://doi.wiley.com/10.1002/2014JC010657 doi: 10.1002/2014JC010657

Cuomo, G., & Guza, R. T. (2017). Infragravity Seiches in a Small Harbor. *Journal of Waterway, Port, Coastal, and Ocean Engineering*, *143*(5), 04017032. doi: 10.1061/(asce)ww.1943-5460.0000392

de Bakker, A. T., Brinkkemper, J. A., van der Steen, F., Tissier, M. F., & Ruessink, B. G. (2016). Cross-shore sand transport by infragravity waves as a function of beach steepness. *Journal of Geophysical Research: Earth Surface*, *121*(10), 1786–1799. doi: 10.1002/2016JF003878

De Bakker, A. T. M., Tissier, M. F. S., & Ruessink, B. G. (2014, 1). Shoreline dissipation of infragravity waves. *Continental Shelf Research*, *72*, 73–82. Retrieved from http://linkinghub.elsevier.com/retrieve/pii/S0278434313003786 doi: 10.1016/j.csr.2013.11.013

de Jong, M. P., & Battjes, J. A. (2004). Low-frequency sea waves generated by atmospheric convection cells. *Journal of Geophysical Research: Oceans*, *109*(1), 1–18. doi: 10.1029/2003jc001931

Gallagher, B. (1971). Generation of surf beat by non-linear wave interactions. *Journal of Fluid Mechanics*, *49*(1), 1–20. doi: 10.1017/S0022112071001897

Guza, R. T., & Thornton, E. B. (1985). Observations of surf beat. *Journal of Geophysical Research*, *90*(C2), 3161–3172. Retrieved from http://doi.wiley.com/10.1029/JC090iC02p03161 doi: 10.1029/JC090iC02p03161

Hasselmann, K. (1962, 4). On the non-linear energy transfer in a gravity-wave spectrum: Part 1. General theory. *Journal of Fluid Mechanics*, *12*(4), 481–500. Retrieved from http://journals.cambridge.org/production/action/cjoGetFulltext?fulltextid=368683http://www.journals.cambridge.org/abstract_S0022112062000373 doi: 10.1017/S0022112062000373

Hasselmann, K., Barnett, T. P., Bouws, E., Carlson, H., Cartwright, D. E., Enke, K., ... Walden, H. (1973). Measurements of wind-wave growth and swell decay during the Joint North Sea Wave Project (JONSWAP). *Ergänzungsheft zur Deutschen Hydrographischen Zeitschrift*, *A8*(12).

Henderson, S. M., & Bowen, A. J. (2002). Observations of surf beat forcing and dissipation. *Journal of Geophysical Research*, *107*(C11). Retrieved from http://doi.wiley.com/10.1029/2000JC000498 doi: 10.1029/2000JC000498

Herbers, T. H. C., Elgar, S., & Guza, R. T. (1995). Generation and propagation of infragravity waves. *Journal of Geophysical Research*, *100*(C12), 24863–24872. Retrieved from http://onlinelibrary.wiley.com/doi/10.1029/95JC02680/fullhttp://doi.wiley.com/10.1029/95JC02680 doi: 10.1029/95JC02680

Herbers, T. H. C., Elgar, S., Guza, R. T., & O'Reilly, W. C. (1995, 6). Infragravity-Frequency (0.005–0.05 Hz) Motions on the Shelf. Part II: Free Waves. *Journal of Physical Oceanography*, *25*(6), 1063–1079. Retrieved from http://journals.ametsoc.org/doi/abs/10.1175/1520-0485(1995)025<1063:IFHMOT>2.0.CO;2#.U_xzxkbkwr4.mendeleyhttp://journals.ametsoc.org/doi/abs/10.1175/1520-0485(1995)025<1063:IFHMOT>2.0.CO;2 doi: 10.1175/1520-0485(1995)025⟨1063:IFHMOT⟩2.0.CO;2

Hersbach, H., Bell, B., Berrisford, P., Hirahara, S., Horányi, A., Muñoz-Sabater, J., ... Thépaut, J. N. (2020). The ERA5 global reanalysis. *Quarterly Journal of the Royal Meteorological Society*, *146*(730), 1999–2049. doi: 10.1002/qj.3803

Li, S., Liao, Z., Liu, Y., & Zou, Q. (2020). Evolution of Infragravity Waves Over a Shoal Under Nonbreaking Conditions. *Journal of Geophysical Research: Oceans*, *125*(8), 1–15. doi: 10.1029/2019JC015864

Longuet-Higgins, M. S., & Stewart, R. W. (1962, 3). Radiation stress and mass transport in gravity waves, with application to 'surf beats'. *Journal of Fluid Mechanics*, *13*(4), 481–504. Retrieved from http://www.journals.cambridge.org/abstract_S0022112062000877http://www.journals.cambridge.org/abstract%7B_%7DS0022112062000877 doi: 10.1017/S0022112062000877

Matsuba, Y., Shimozono, T., & Sato, S. (2020). Wave-breaking modulation by infragravity waves during an extreme typhoon. *PLoS ONE*, *15*(4), 1–14. Retrieved from http://dx.doi.org/10.1371/journal.pone.0231242 doi: 10.1371/journal.pone.0231242

Mei, C. C., & Benmoussa, C. (1984, 4). Long waves induced by short-wave groups over an uneven bottom. *Journal of Fluid Mechanics*, *139*, 219. Retrieved from http://journals.cambridge.org/abstract_S0022112084000331http://www.journals.cambridge.org/abstract_S0022112084000331 doi: 10.1017/S0022112084000331

Molin, B. (1982). *On the generation of long-period second order free waves due to changes in the bottom profile* (Tech. Rep.). Tokyo, Japan.

Neale, J., Harmon, N., & Srokosz, M. (2015, 9). Source regions and reflection of infragravity waves offshore of the ¡scp¿U¡/scp¿ . ¡scp¿S¡/scp¿ .s ¡scp¿P¡/scp¿ acific ¡scp¿N¡/scp¿ orthwest. *Journal of Geophysical Research: Oceans*, *120*(9), 6474–6491. Retrieved from https://onlinelibrary.wiley.com/doi/abs/10.1002/2015JC010891 doi: 10.1002/2015JC010891

Okihiro, M., Guza, R. T., & Seymour, R. J. (1992). Bound infragravity waves. *Journal of Geophysical Research*, *97*(C7), 11453–11469. Retrieved from http://onlinelibrary.wiley.com/doi/10.1029/92JC00270/fullhttp://doi.wiley.com/10.1029/92JC00270 doi: 10.1029/92JC00270

Okihiro, M., Guza, R. T., & Seymour, R. J. (1993). Excitation of seiche observed in a small harbor. *Journal of Geophysical Research*, *98*(C10), 18201–18211. Retrieved from http://doi.wiley.com/10.1029/93JC01760 doi: 10.1029/93JC01760

Pomeroy, A., Lowe, R., Symonds, G., Van Dongeren, A., & Moore, C. (2012, 11). The dynamics of infragravity wave transformation over a fringing reef. *Journal of Geophysical Research*, *117*(C11). Retrieved from http://doi.wiley.com/10.1029/2012JC008310 doi: 10.1029/2012JC008310

Rawat, A., Ardhuin, F., Ballu, V., Crawford, W., Corela, C., & Aucan, J. (2014, 11). Infragravity waves across the oceans. *Geophysical Research Letters*, *41*(22), 7957–7963. Retrieved from http://doi.wiley.com/10.1002/2014GL061604 doi: 10.1002/2014GL061604

Reniers, A. J. H. M., Naporowski, R., Tissier, M. F. S., de Schipper, M. A., Akrish, G., & Rijnsdorp, D. P. (2021, 1). North Sea Infragravity Wave Observations. *Journal of Marine Science and Engineering*, *9*(2), 141. Retrieved from https://www.mdpi.com/2077-1312/9/2/141 doi: 10.3390/jmse9020141

Rhie, J., & Romanowicz, B. (2006). A study of the relation between ocean storms and the Earth's hum. *Geochemistry, Geophysics, Geosystems*, *7*(10). doi: 10.1029/2006GC001274

Russell, P. E. (1993, 11). Mechanisms for beach erosion during storms. *Continental Shelf Research*, *13*(11), 1243–1265. Retrieved from http://www.sciencedirect.com/science/article/pii/027843439390051Xhttp://linkinghub.elsevier.com/retrieve/pii/027843439390051X doi: 10.1016/0278-4343(93)90051-X

Sheremet, A., Staples, T., Ardhuin, F., Suanez, S., & Fichaut, B. (2014, 1). Observations of large infragravity-wave run-up at Banneg Island, France. *Geophysical Research Letters*. Retrieved from http://dx.doi.org/10.1002/2013GL058880 doi: 10.1002/2013GL058880

Smit, P. B., Janssen, T. T., Herbers, T. H. C., Taira, T., & Romanowicz, B. A. (2018, 7). Infragravity Wave Radiation Across the Shelf Break. *Journal of Geophysical Research: Oceans*, *123*(7), 4483–4490. Retrieved from http://doi.wiley.com/10.1029/2018JC013986 doi: 10.1029/2018JC013986

Sugioka, H., Fukao, Y., & Kanazawa, T. (2010). Evidence for infragravity wave-tide resonance in deep oceans. *Nature Communications*, *1*(7), 1–7. doi: 10.1038/ncomms1083

Symonds, G., Huntley, D. A., & Bowen, A. J. (1982). Two-dimensional surf beat: Long wave generation by a time-varying breakpoint. *Journal of Geophysical Research*, *87*(C1), 492–498. Retrieved from http://onlinelibrary.wiley.com/doi/10.1029/JC087iC01p00492/fullhttp://doi.wiley.com/10.1029/JC087iC01p00492 doi: 10.1029/JC087iC01p00492

Thotagamuwage, D. T., & Pattiaratchi, C. B. (2014, 9). Influence of offshore topography on infragravity period oscillations in Two Rocks Marina, Western Australia. *Coastal Engineering*, *91*, 220–230. Retrieved from http://www.sciencedirect.com/science/article/pii/S0378383914001197 doi: 10.1016/j.coastaleng.2014.05.011

Van der Molen, W., Monardez, P., & Van Dongeren, A. (2006, 3). Numerical simulation of long-period waves and ship motions in Tomakomai port, Japan. *Coastal Engineering Journal*, *48*(1), 59–79. Retrieved from http://www.worldscientific.com/doi/abs/10.1142/S0578563406001301 doi: 10.1142/S0578563406001301

van der Molen, W., Scott, D., Taylor, D., & Elliott, T. (2016). Improvement of mooring configurations in Geraldton harbour. *Journal of Marine Science and Engineering*, *4*(1), 1–20. doi: 10.3390/jmse4010003

Van Dongeren, A., Battjes, J., Janssen, T., van Noorloos, J., Steenhauer, K., Steenbergen, G., & Reniers, A. (2007, 2). Shoaling and shoreline dissipation of low-frequency waves. *Journal of Geophysical Research*, *112*(C2).

Retrieved from http://doi.wiley.com/10.1029/2006JC003701 doi: 10.1029/2006JC003701

Van Thiel de Vries, J. S. M., Van Gent, M. R. A., Walstra, D. J. R., & Reniers, A. J. H. M. (2008, 12). Analysis of dune erosion processes in large-scale flume experiments. *Coastal Engineering*, *55*(12), 1028–1040. Retrieved from http://linkinghub.elsevier.com/retrieve/pii/S0378383908000860 doi: 10.1016/j.coastaleng.2008.04.004

Vrećica, T., Soffer, R., & Toledo, Y. (2019, 8). Infragravity Wave Generation by Wind Gusts. *Geophysical Research Letters*, *46*(16), 9728–9738. Retrieved from https://onlinelibrary.wiley.com/doi/abs/10.1029/2019GL084241https://onlinelibrary.wiley.com/doi/10.1029/2019GL084241 doi: 10.1029/2019GL084241

Webb, S. C. (2007). The Earth's 'hum' is driven by ocean waves over the continental shelves. *Nature*, *445*(7129), 754–756. doi: 10.1038/nature05536

Webb, S. C., Zhang, X., & Crawford, W. (1991). Infragravity waves in the deep ocean. *Journal of Geophysical Research*, *96*(C2), 2723–2736. Retrieved from http://doi.wiley.com/10.1029/90JC02212 doi: 10.1029/90JC02212

Zijlema, M., Van Vledder, G. P., & Holthuijsen, L. H. (2012). Bottom friction and wind drag for wave models. *Coastal Engineering*, *65*, 19–26. Retrieved from http://dx.doi.org/10.1016/j.coastaleng.2012.03.002 doi: 10.1016/j.coastaleng.2012.03.002

539 ## Figures

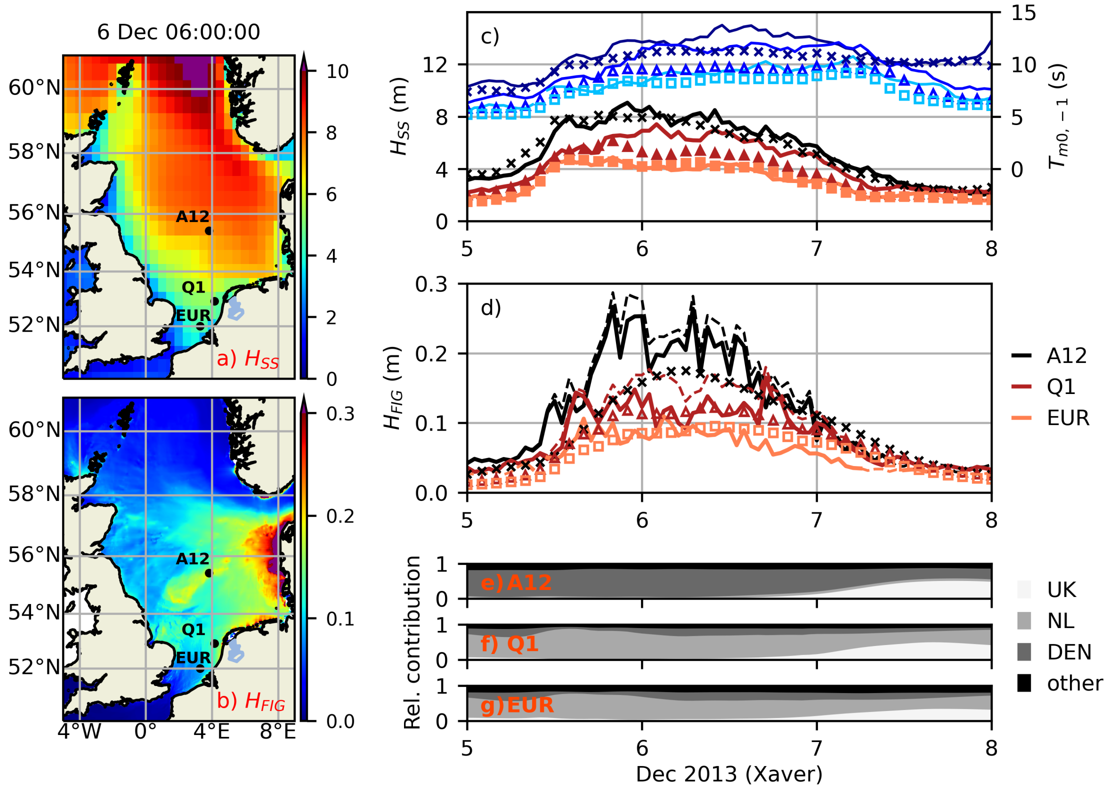

Figure 1. Infragravity wave conditions in the North Sea during storm Xaver (5-8 Dec 2013). Snapshot of the instantaneous significant SS wave height H_{SS} from the ERA5 reanalysis (panel a) and FIG wave height H_{FIG} from the SWAN model (panel b) at 6 Dec 06:00:00 UTC. Observed (lines) and ERA5 (markers) time-series of H_{SS} (full line and filled markers, left axis) and $T_{m0,-1}$ (dashed lines and open markers, right axis) at three stations in the southern North Sea (A12, Q1 and EUR) (panel c). Observed (full lines) and SWAN (markers) FIG wave heights H_{FIG} at A12, Q1 and EUR (panel d). The dashed lines in panel d represent the observations of the total IG wave height (including both bound and free contributions). Relative contribution of different shorelines to the SWAN predicted FIG variance ($\propto \quad H_{FIG}^2$) at the three stations (panel e-g).

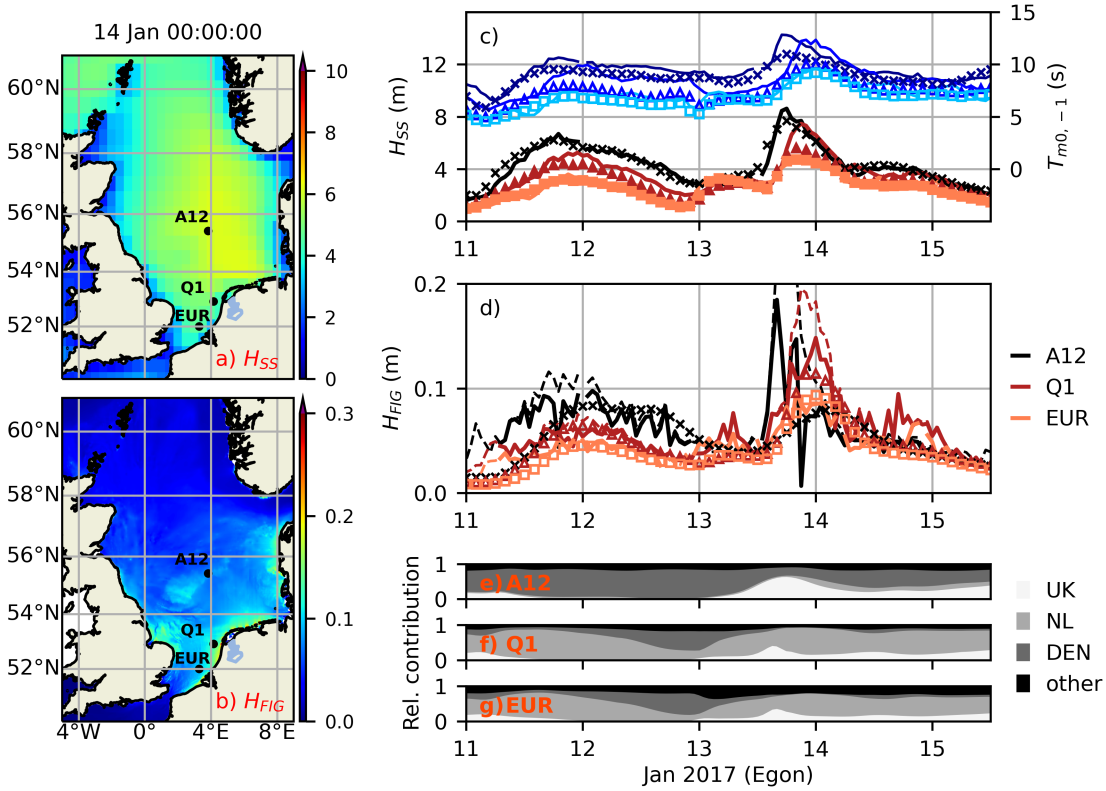

Figure 2. Infragravity wave conditions in the North Sea prior to and during storm Egon (13-15 Jan 2017). Refer to the caption of Fig. 1 for further details.

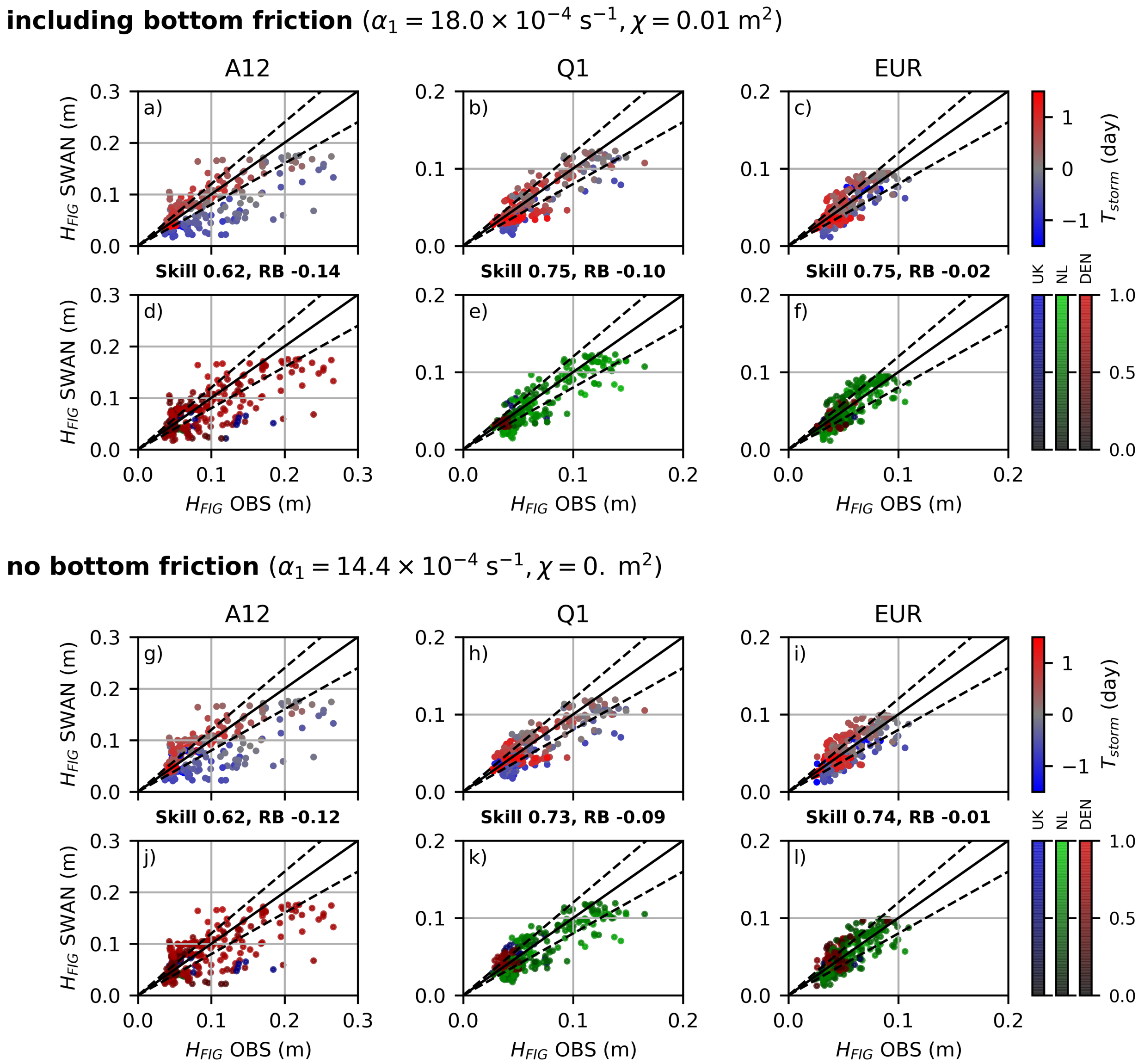

Figure 3. Scatter plot of the instantaneous observed (OBS) versus modelled (SWAN) FIG wave height H_{FIG} at station A12 (left panels), Q1 (middle panels) and EUR (right panels). The top plots (panel a-f) show the modelling results excluding the effect of bottom friction, and the bottom plots (panel g-l) show the results including bottom friction. In panels (a-c) and (g-i), the marker colour indicates the time relative to the approximate peak in the observed H_{FIG} at A12. In panels (d-f) and (j-l), the marker colour indicates the region from which the majority of the IG variance ($\propto H_{FIG}^2$) originated. The colour shading indicates the relative contribution of this region to the total IG variance, with darker colors indicative for significant contributions from multiple regions. Two statistical parameters to quantify the model-data comparison are shown for all stations. The model skill is computed as Skill $= 1 - \frac{\sqrt{\frac{1}{N}\sum(H^o_{FIG} - H^c_{FIG})^2}}{\sqrt{\frac{1}{N}\sum(H^o_{FIG})^2}}$, and the relative bias is computed as RB $= \frac{\sum(H^c_{FIG} - H^o_{FIG})}{\sum H^o_{FIG}}$, where N is the total number of samples and superscripts o and c indicate an observed and computed variable, respectively.

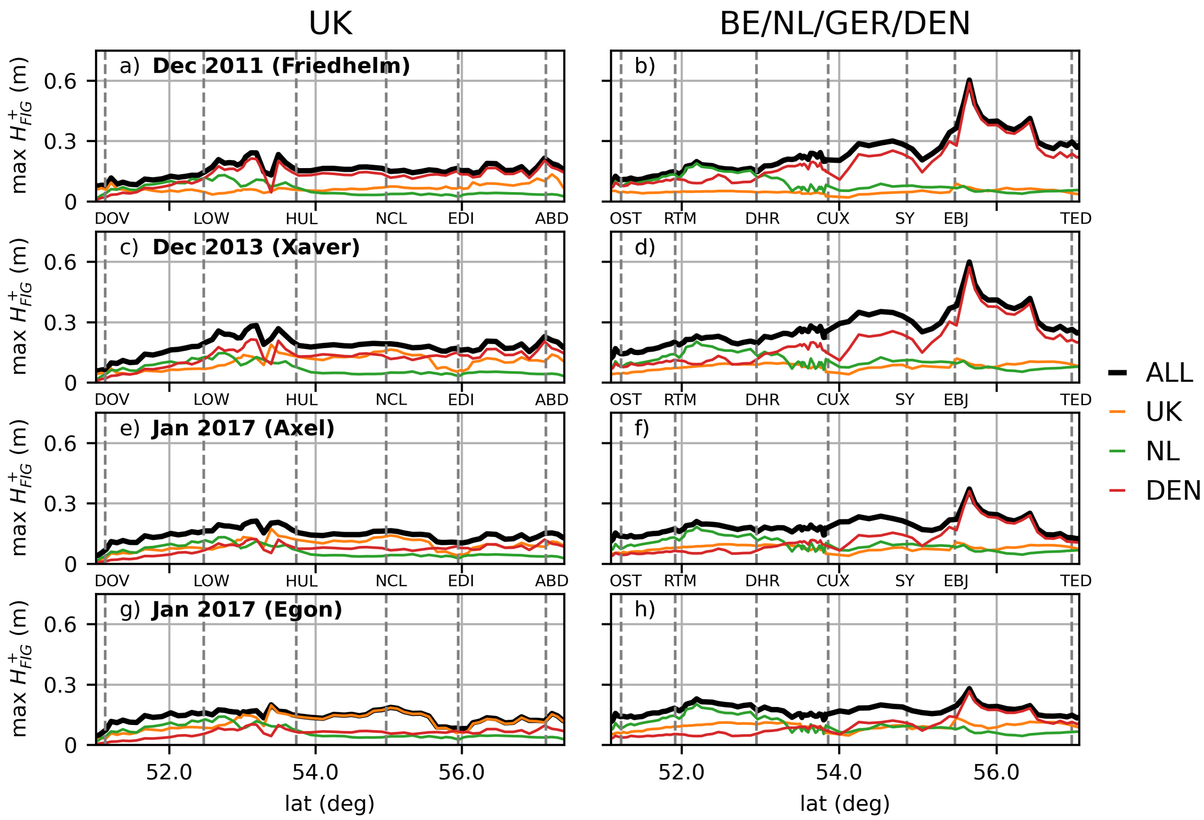

Figure 4. Maximum of the SWAN modelled (including bottom friction) shoreward directed FIG wave height H^+_{FIG} (black line) during individual storm events along the Eastern UK coastline (left panels) and the coastlines between the Belgium and Denmark (right panels) at approximately 20 m water depth. The coloured lines indicate the H^+_{FIG} that was radiated from the UK, Dutch (NL) or Danish (DEN) coast (as indicated by the legend). The vertical dashed lines indicate geographical locations along the coastline. Left panels: DOV (Dover), LOW (Lowestoft), Hul (Hull), NCL (Newcastle), EDI (Edingburgh), ABD (Aberdeen); Right panels: OST (Ostend), RTM (Rotterdam), DHR (Den Helder), CUX (Cuxhaven), SY (Sylt), EBJ (Esbjerg), TED (Thisted).

Supporting Information for "Free infragravity waves in the North Sea"

Dirk P. Rijnsdorp[1], Ad J. H. M. Reniers[1], Marcel Zijlema[1]

[1]Environmental Fluid Mechanics section, department of Hydraulic Engineering, Faculty of Civil Engineering and Geosciences, Delft University of Technology, Delft, the Netherlands

Contents of this file

Figures S1 to S2

Introduction

This supporting information provides the details and results of the model sensitivity study (spatial and directional resolution) and the model calibration study.

Model sensitivity study (spatial and directional resolution)

A sensitivity study was conducted to determine the optimal spatial and directional resolution of the SWAN simulations. A stationary simulation (with the 1$^{\text{st}}$ order BSBT propagation scheme) was ran with all shorelines along the North Sea radiating an equal amount of IG energy. The grid and directional resolution were varied and compared with a reference simulation. The reference simulation was run with the 2$^{\text{nd}}$ order SORDUP propagation scheme and with the finest considered spatial and directional resolution. The directional resolution was varied between $2° - 15°$ and the longitudinal grid resolution was varied between $0.01 - 0.05°$. The latitudinal resolution was kept as a constant fraction (≈ 1.5) of the longitudinal resolution. For each simulation, we compute the model skill relative to the reference simulation for the free infragravity wave height H_{FIG} at the three measurement stations ($N = 3$),

$$Skill = 1 - \frac{\sqrt{\frac{1}{N}\sum (H_{FIG} - H_{FIG,R})^2}}{\sqrt{\frac{1}{N}\sum H_{FIG,R}^2}}, \quad (1)$$

where subscript R is indicative for the reference simulation.

This sensitivity study showed that the model results were only weakly affected by the directional and grid resolution (Fig. S1). Based on these results, the model simulations were conducted with a resolution of 0.025° in longitudinal and 0.0165° in latitudinal direction, and a directional resolution $\Delta\theta = 8°$.

Model calibration study (α_1 and χ)

Following the model sensitivity study, a calibration study was conducted to decide the α_1 parameter of the infragravity source term, and the χ parameter of the JONSWAP friction formulation. For this purpose, we conducted a non-stationary simulation of storm Friedhelm. During storm Friedhelm, significant sea-swell waves mainly made landfall in Denmark, and modelled H_{FIG} in the North Sea were dominated by infragravity waves radiated from the Danish coast. This allowed for a more straightforward model calibration compared to a storm during which H_{FIG} originated from multiple coastal sections.

First, we selected the α_1 parameter based on the model-data agreement at station A12 for the simulation without bottom friction. This resulted in $\alpha_1 = 14.4 \times 10^{-4}$ s^{-1}. Without friction, H_{FIG} is slightly over predicted at station EUR (Fig. S2). Subsequently, we varied α_1 and χ to 1) math the predictions without bottom friction at A12, and 2) improve the model-data agreement at station EUR. This resulted in $\alpha_1 = 18\times10^{-4}$ s^{-1} and $\chi = 0.01$ m^2. As the model-data agreement with these model parameters was satisfactory for the other storms, we made no attempt to optimize the model results by calibrating α_1 for separate coastal sections.

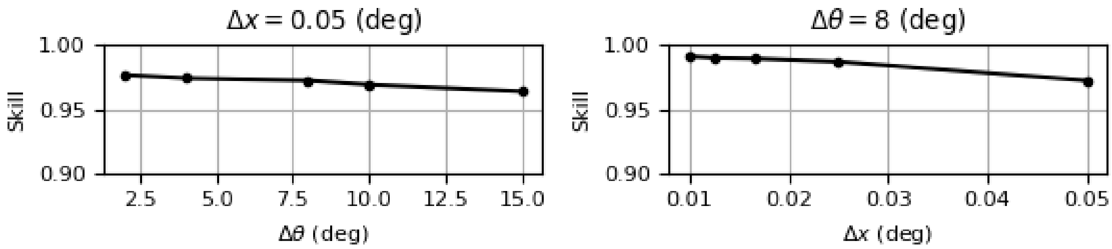

Figure S1. Model skill for a varying directional resolution ($\Delta\theta$) with a fixed grid resolution (with Δx the longitudinal resolution) (left panel), and for a varying grid resolution with a fixed directional resolution (right panel).

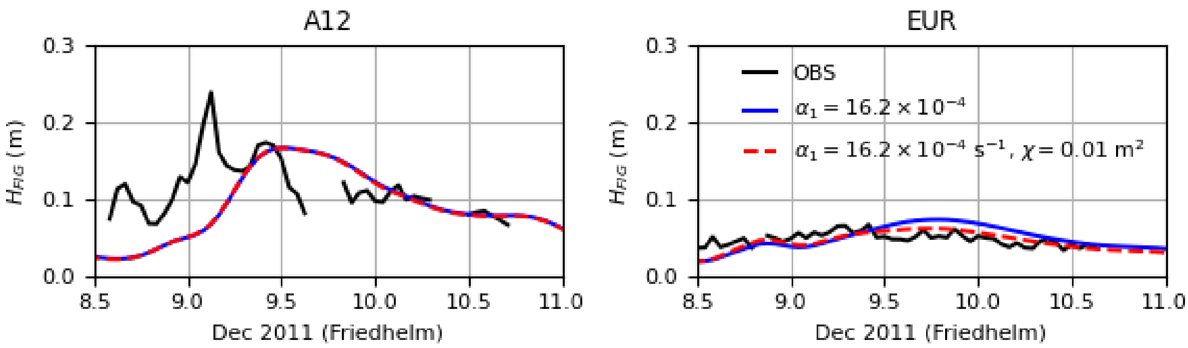

Figure S2. Observed (black line) and predicted (excluding friction, blue line; and including friction, red line) infragravity wave height H_{FIG} at station A12 in the central North Sea (left panel) and station EUR in the southern North Sea (right panel) during storm Friedhelm.